

Modelling drying shrinkage in reconstructed porous materials: application to porous Vycor glass

Dale P Bentz[†], Edward J Garboczi[†] and Daniel A Quenard[‡]

[†] National Institute of Standards and Technology, Gaithersburg, MD 20899, USA

[‡] Centre Scientifique et Technique du Batiment, 38400 Saint-Martin d'Heres, France

Received 8 September 1997, accepted for publication 22 January 1998

Abstract. A three-dimensional representation of the microstructure of porous Vycor glass was generated from a transmission electron micrograph, and was analysed to compute the locations of all capillary-condensed water as a function of relative humidity. On solid surfaces where capillary-condensed water was not present, an adsorbed water layer, whose thickness is a function of relative humidity, was placed. As a function of relative humidity, fixed pressures were specified in all capillary-condensed water, and the change in specific surface free energy with relative humidity was taken into account for the adsorbed water layers. New finite-element codes were developed to determine the drying shrinkage, in response to the changes in the specific surface free energy of the adsorbed water layers and to the fixed pressures in the capillary condensed water. Existing finite-element and finite-difference codes were used to evaluate the elastic moduli, the electrical and thermal conductivity, and the fluid permeability of the material. Bulk properties such as fluid permeability and electrical and thermal conductivity agreed well with experiment. By adjusting the elastic moduli of the solid backbone, which are not experimentally determined quantities, the computed porous glass elastic moduli, and computed low and high relative humidity shrinkage all agreed well ($\leq 10\%$) with experimental values. At intermediate relative humidities, the agreement for shrinkage was worse, partly due to inaccuracies in the simulated water desorption curve, and partly due to the fact that water-induced swelling of the solid backbone, an effect that is probably present in the real material, was not taken into account in the model computations.

1. Introduction

The phenomenon of drying shrinkage in porous materials is relevant to a variety of problems of technological interest such as the shrinkage [1] and cracking [2] of concrete, and the drying of gels and aerogels [3]. In these porous materials, pore diameters are often such that capillary condensation will occur over some range of partial pressure of the gas phase of the adsorbent considered. The saturation, which is defined as the fraction of the pore space filled with liquid phase, of these materials is therefore a strong function of the external partial pressure of the gas phase. The capillary tension induced by the condensed fluid will generate stresses at all fluid–solid interfaces, resulting in some deformation of the solid phase and hence an overall shrinkage in the composite. In addition, changes in specific surface free energy [4,5] in adsorbed fluid layers can also contribute to the overall shrinkage, especially at lower partial pressures. In this paper, we focus on the fluid being water, although the techniques described are general. The partial pressure of water vapour at a given temperature, divided by the saturated water vapour pressure at the same temperature, is usually called the relative humidity (RH).

While many measurements of shrinkage have been made, a direct linkage between microstructure and shrinkage is still lacking. Mackenzie [6] has presented a general analytical method for estimating the dilatation of porous materials based on their elastic properties and the amount of water-filled porosity at a given relative humidity. This approach is exact for a saturated porous material, but only approximate for partially saturated materials. In addition, a continuum approach to the general elastic dynamics of unsaturated and fluid-saturated porous materials has been extensively discussed by Biot [7].

In this paper, a computer modelling approach is presented in which the shrinkage behaviour of a three-dimensional microstructure is directly computed. Beginning with a discrete three-dimensional representation of microstructure, a previously developed algorithm based on the Kelvin–Laplace equation [1] is used to estimate the equilibrium location of all capillary-condensed water at some fixed relative humidity. In addition, the surface energy and thickness of the water layer adsorbed on all exposed (no capillary condensation) solid surfaces is estimated. A new finite-element analysis method is then employed to compute the shrinkage of the three-dimensional (3D) composite, which is caused by the capillary tension present in the condensed water and the surface energy changes in the adsorbed water. It should be noted that the techniques developed in this paper do not deal with the dynamics of the shrinkage process or flow of the water during shrinkage, but only estimate the final equilibrium value of shrinkage. Thus, for example, it is implicitly assumed that the shrinkage does not alter the microstructure enough to significantly change the locations of the capillary-condensed water at the resolution being considered. For the magnitude of the shrinkage strains considered, 0.001 or less, this is a reasonable assumption.

Other physical properties besides shrinkage depend on microstructure, too, of course. One way to test the accuracy of the reconstructed microstructures is to compute their physical properties and compare to experimental measurements on equivalent systems. By comparing to experimental data for real materials, where possible, we hope to indicate precisely the advantages and limitations of the 3D media that are reconstructed from 2D images using our algorithm.

There are several reasons why porous Vycor has been chosen as a material upon which to test these techniques. First, the total porosity and pore surface area of porous Vycor glass are similar to those of hardened cement paste, which is our ultimate research interest [1], and the shrinkage strains found in this material, of the order of 0.001, match the approximate tensile fracture strain [2] of cement-based materials. More important, however, is the fact that many of the properties of porous Vycor glass are readily available [8], as are experimental measurements of porous Vycor shrinkage against external relative humidity [9]. Also, the drying shrinkage of porous Vycor, in both low [5, 8] and high [9] partial pressure of absorbent regimes, has been shown to be well described by linear elastic equations [5, 8, 9], so that the finite-element analysis can also be simplified to be linear elastic only. This is unfortunately not the case in hardened cement paste [1], which is strongly viscoelastic. Because of all of the above reasons, porous Vycor glass has been chosen to test our reconstruction algorithm [10] and demonstrate our new shrinkage algorithm.

2. Computational and experimental techniques

2.1. Microstructure generation

The microstructure reconstruction algorithm has previously been fully described [10], so that only a brief treatment is given here. The 3D digital image structure generated is

limited to 100^3 or 200^3 pixels in volume, with periodic boundaries employed to reduce surface errors. Larger images can be generated, but the programs that compute quantities like elastic moduli, fluid permeability, and electrical and thermal conductivities, are much more computer memory intensive, and so 100^3 to 200^3 are the largest images used at present. We use a filtering function, applied to a 3D random noise image, that is based on correlation analysis of a real 2D image of the porous glass microstructure. Algorithms with some similarities to ours have been previously used for porous Vycor [11], which employed the filtering of a random white-noise image with the convolution of a Laplacian and a Gaussian function. Alternate generation techniques for porous Vycor based on spinodal decomposition [12], an ‘intersecting growth mechanism’ [13], and phase separation in a 3D Ising model [14] have also been previously presented, although not with the extensive testing of properties given in this paper.

Starting with a 2D binary image of porous Vycor [15], the 2D autocorrelation function for the pore phase is determined. If the $M \times N$ pixel 2D image is defined as a discrete valued function, $I(x, y)$, where $I(x, y)$ is equal to one for pore pixels and zero for solid pixels, the two-point correlation function for the porosity is given by [16]

$$S(x, y) = \sum_{i=1}^{M-x} \sum_{j=1}^{N-y} \frac{I(i, j)I(i+x, j+y)}{(M-x)(N-y)}. \quad (1)$$

The function $S(x, y)$ is then converted to its polar form and averaged over all orientations to obtain $S(r)$. Finally, the autocorrelation function, $F(r)$, for the porosity is defined by [17]

$$F(r) = F(x, y, z) = \frac{[S(r) - S(0)S(0)]}{[S(0) - S(0)S(0)]}. \quad (2)$$

By definition, $F(0) = 1$ and $F(r) \rightarrow 0$ as $r \rightarrow \infty$, since $S(r) \rightarrow [S(0)]^2$ as $r \rightarrow \infty$. For an isotropic, random material like porous Vycor, $F(r)$ is nearly zero for r of the order of a few times the largest pore size.

Since, for a large enough image of an isotropic material, the autocorrelation function will be the same in two and three dimensions, it can be used to filter a 3D image of white noise [18]. For a finite size image, there will of course be some slice-to-slice fluctuation. For the size image considered here, these fluctuations were negligible. After the filtering process, a grey scale image is obtained. A threshold grey scale is then chosen, such that all pixels with grey level above and below this threshold are set to either solid or pore. This threshold grey scale is such that a 3D binary image is created in which the porosity matches that of the original 2D image.

Finally, a surface rearrangement algorithm based on analysis of local curvature [19–21] is used to alter the hydraulic radius (the ratio of pore volume to pore surface area) of the computed 3D structure. Usually the hydraulic radius is adjusted so as to match that measured for the original 2D image [10], providing a 3D computer representation of the material microstructure with the correct porosity and pore surface area. However, it is known that porous Vycor glass is a variable material, with a variable pore size and surface area. In the literature, values for the nitrogen BET surface area range from $100 \text{ m}^2 \text{ g}^{-1}$ [15] all the way up to $173 \text{ m}^2 \text{ g}^{-1}$ [5]. We have had to generate 3D images with different surface areas in order to be able to accurately compare with experiments, as many properties are sensitively dependent on surface area, or, equivalently, since the porosity is fixed, on hydraulic radius and pore size. This may be easily done using the surface rearrangement algorithm. A portion of a computed 3D microstructure of the porous Vycor glass is provided in figure 1, with a surface area of $70 \text{ m}^2 \text{ g}^{-1}$. It is important to note that the scale of the

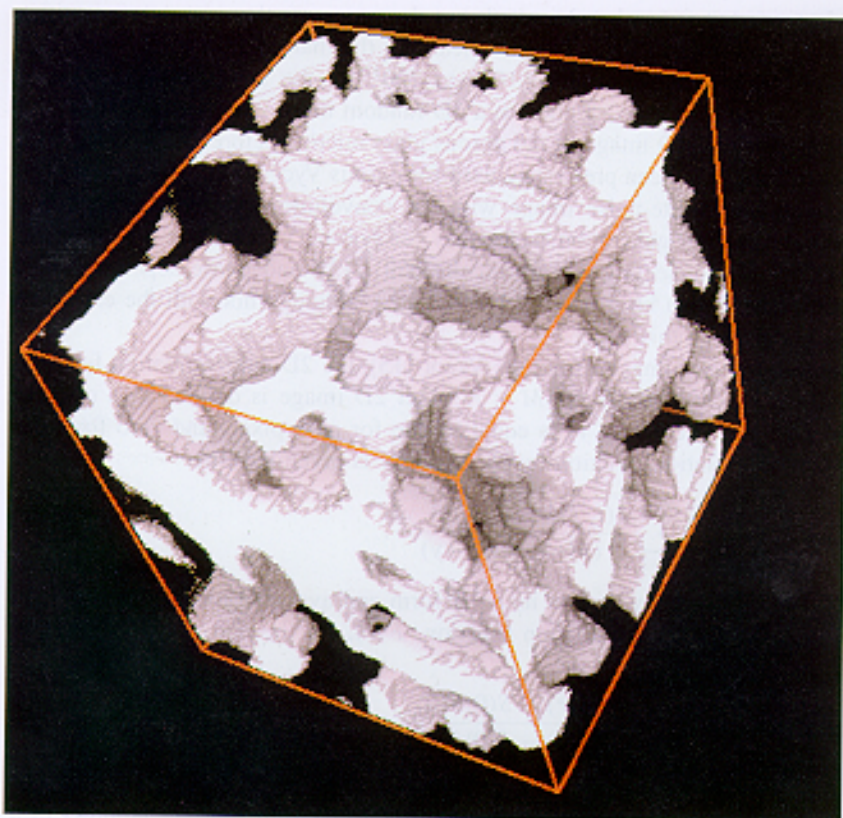


Figure 1. A reconstructed 3D image of porous Vycor glass. Pores are shown in white or grey, while solids are transparent. The scale is roughly 1 nm/pixel, and the image is 100^3 pixels in size.

original transmission electron micrograph (TEM) used [15], and therefore the scale of the resulting generated 3D image, is approximately 1 nm per pixel, so that features smaller than this have been smoothed out and lost [8]. To convert the measured specific surface area in the model from m^{-1} to $\text{m}^2 \text{g}^{-1}$, we are assuming that the density of the backbone is approximately that of fused silica, $2.18 \times 10^6 \text{ g m}^{-3}$ [8].

2.2. Modelling of sorption processes

Once a 3D representation of the solid and pore phases in the material has been generated, the next step is to determine the location of the capillary-condensed water as a function of relative humidity, given that there is an adsorbed water layer on all solid surfaces. To analyse the capillary water content, a geometrical algorithm [1] is employed that is based on the Kelvin–Laplace equation:

$$\ln(P/P_0) = \frac{KV_m\gamma_T}{RT} \quad (3)$$

where P is the vapour pressure of a liquid surface of average curvature K ($K < 0$), γ_T is the liquid surface tension, V_m its molar volume, T is the absolute temperature, R is the

universal gas constant, and P_0 is the vapour pressure for a planar surface ($K = 0$) at standard conditions. For water, $\gamma_f = 0.07 \text{ N m}^{-2}$ and $V_m = 1.8 \times 10^{-5} \text{ m}^3 \text{ mol}^{-1}$, while $R = 8.314 \text{ J mol}^{-1} \text{ K}^{-1}$, and T was taken to be approximately the same as was used in experiment [9], 300 K. The dimensionless ratio P/P_0 defines the relative humidity. Based on equation (3), sorption can be *approximately* simulated at a given relative humidity using a geometrical criterion that determines all of the locations in the pore space where a digitized sphere of radius r can be placed without overlapping any of the solid phase. In this case, $K = -2/r$ (concave meniscus), so that equation (3) gives the vapour pressure of a meniscus of radius r . These locations are removed from consideration as sites for occupation by condensed water at the given value of P/P_0 but not for occupation by an adsorbed layer, and those remaining indicate the locations of the condensed liquid. Using a digitized sphere is of course only an approximation. Any surface has two principal radii of curvature in 3D, so that a variety of ellipsoidal shapes are possible for the air–water interfaces [22–24], which will not be simulated by our algorithm.

For desorption, the above geometrical constraint must be augmented by a connectivity analysis [1]. During desorption, a capillary pore can empty only when its size equals or exceeds the Kelvin–Laplace radius and when it is connected to the exterior of the sample by a pathway consisting exclusively of the same size or larger ‘empty’ pores. Including this connectivity analysis in the simulation of sorption isotherms produces a natural hysteresis in the desorption–adsorption curves similar to that observed experimentally [1]. This geometrical analysis is applied to the porous Vycor microstructures to produce a series of three-phase composites consisting of solid, air-filled pores, and water-filled pores.

As was mentioned above, in order to carry out the sorption computation properly, especially for the smaller pores, it is necessary to first determine the thickness, t , of the adsorbed water layer as a function of relative humidity. Here, we use an empirical equation developed for cement-based materials [25]:

$$t = 0.395 - 0.189 \ln \left[-\ln \left(\frac{P}{P_0} \right) \right] \quad (\text{nm}). \quad (4)$$

Two other $t(\text{RH})$ functions in the literature are actually quite similar to this one [26, 27], so that the choice of function would not make a large difference in the results. In equation (4), the thickness of the water layer is given in nanometres. Computationally, for a given relative humidity, a sorbed water layer n pixels thick ($n = 0$ or 1) was first placed on the solid surfaces (using a dilation algorithm) before executing the geometrical algorithms for sorption described above. Non-integer pixel adsorption thicknesses, x , determined using equation (4), were approximated in a two-step approach. First, the integer value of x , $\text{int}(x)$, dilations were executed, followed by the geometrical sorption algorithm. After sorption, the total amount of water present was incremented by adding the value obtained by multiplying the exposed (to air) surface area remaining after the capillary condensation analysis by the factor $[x - \text{int}(x)]$ [1].

There are some difficulties in using the Kelvin–Laplace equation as described above. Using molecular dynamics and density-functional theory studies of adsorption in a single pore, it was found that equation (3) starts to break down significantly at pore sizes of about 5–10 nm [28–30]. This is the typical pore size in porous Vycor. However, by first considering a water layer on the pore surfaces, before estimating capillary condensation with equation (3), we are in effect using a modified Kelvin–Laplace equation, which has been shown to work somewhat better at smaller pore sizes than the unmodified Kelvin–Laplace equation [29]. Also, we desire to compute adsorption and desorption on a general pore structure represented by a digital image, not on a single model shape pore. The

computational burden would be enormous if Monte Carlo [28] or density functional theory [31] were used to more correctly handle the actual fluid molecular state in pores less than 10 nm in width. In the real pore space that we want to consider, there are no nicely-shaped (slit, cylinder, etc) pores on which to operate these more powerful but more complicated techniques [32]. The simple but approximate geometric technique outlined above can equally well be applied to any type of pore space, and is particularly suited to digital images, which is usually what one has to deal with in looking at real systems.

There is also evidence that the main cause of the hysteresis loop between adsorption and desorption is percolation effects due to the pore network, not the size and shape of individual pores [30,33,34]. In that case, the topology of the pore network will tend to wash out individual pore details that are treated somewhat incorrectly by our algorithm. More discussion of this question will be delayed until section 4.

2.3. Experimental measurement of sorption isotherms for porous silica glass

The sorption isotherms were measured using a hygrogravimetric method [35]. The mass of the sample was continuously recorded in a chamber in which the temperature and the relative humidity were controlled. The required partial pressure of water vapour was produced by mixing dry air and water-saturated air. For adsorption, starting from a relative humidity of around 3%, the relative humidity was increased in a stepwise manner. For both adsorption and desorption, the mass of the sample was allowed to reach a constant value, before the relative humidity was increased or decreased. The relative humidity range of the apparatus was 3 to 98%. It should be noted that differences which exist between experimental curves published in the literature are probably at least partially due to the variability of the porosity and pore structure of porous Vycor glass from one sample to another, and not only differences in experimental techniques. Computationally, we have noticed large differences in sorption/desorption for different surface area models, as the hydraulic radius, for a fixed porosity, acts as a length scale for the pore sizes in the pore space, which of course will greatly affect the amount of water present at a given RH value. The surface area of the experimental sample used was not measured, but was probably somewhere between 100 and 200 m² g⁻¹, typical for porous Vycor.

2.4. Computation of capillary pressure and change in specific surface free energy

To compute the shrinkage due to capillary condensed water, it is necessary to specify the stresses present in this water in the microstructure. The hydrostatic pressure or capillary tension in the capillary-condensed water is given by the simple expression

$$\sigma_{\text{cap}} = K \gamma_f \quad (5)$$

where for a given relative humidity, K is calculated using equation (3).

The shrinkage due to the surface adsorbed water (Bangham shrinkage [36]) is based on the specific surface free energy (J m⁻²) change that occurs as the thickness of this adsorbed layer changes. This change is given by the Gibbs adsorption equation in the form [37]

$$\Delta \gamma_s = - \frac{RT}{V_m} \int_{P_0}^P t \, d \left(\ln \left(\frac{P}{P_0} \right) \right) \quad (6)$$

where P is less than P_0 . The zero point for the surface free energy can be taken to be at 100% relative humidity, in order to convert $\Delta \gamma_s$ to γ_s . The zero point is arbitrary, as

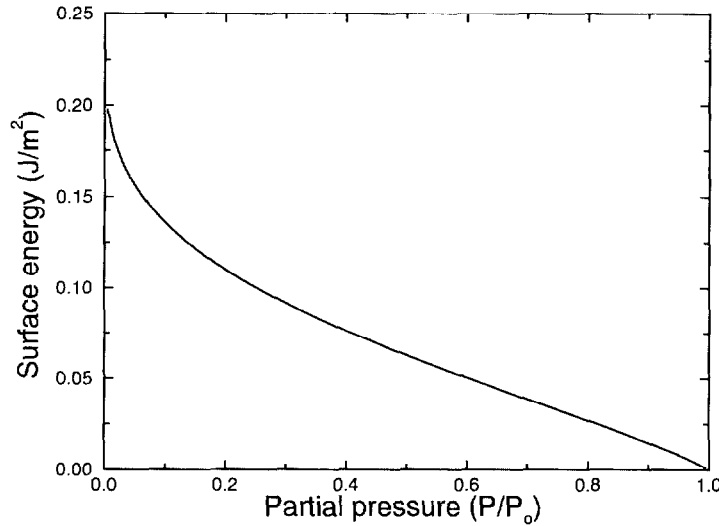


Figure 2. The computed change in surface energy as a function of relative humidity from equation (7) in the text.

only the change in surface energy is physically meaningful. The expression for t given in equation (4) was substituted into (6) and the integral then computed to give

$$\gamma_s \left(\frac{P}{P_0} \right) = \frac{-10^{-9} RT}{V_m} \left[0.584 \ln \left(\frac{P}{P_0} \right) - 0.189 \ln \left(\frac{P}{P_0} \right) \ln \left(-\ln \left(\frac{P}{P_0} \right) \right) \right]. \quad (7)$$

Figure 2 provides a plot of γ_s against relative humidity determined using (7). In figure 2, at zero RH, the surface free energy is about 0.2 J m^{-2} . In Iler [38], the surface energy of a fully hydroxylated silica surface is given as 0.13 J m^{-2} , while for a fully dehydroxylated surface the surface energy is about 0.26 J m^{-2} . For the porous Vycor material being considered, the value of 0.2 J m^{-2} falls in between these values, which is a reasonable result, as the surfaces in Vycor are probably not at either of these two extreme hydroxylation points [8].

2.5. Finite-element technique for shrinkage and elastic moduli

Once a model microstructure has been generated, it can then be analysed using a finite-element technique especially adapted to digital images. In this technique, each cubic pixel in the 3D image is taken to be a tri-linear finite element, which results in a finite-element problem with as many nodes as there were pixels in the original image. This is a large computational problem, too large for a direct solver like a Gaussian elimination method, and so requires a relaxation solution method like the conjugate gradient algorithm [39].

To find the elastic moduli of a model microstructure, periodic boundary conditions are applied that incorporate a fixed applied strain. The numerical solution (minimum elastic energy) for the displacements is found [40], and the elastic moduli are simply given by the average stress found in the problem, in the usual way of composite theory [39, 41].

Computing the shrinkage due to internal forces is somewhat more complicated, requiring extensions to the basic 3D digital image finite-element method. In this case, the overall size and shape of the system must be made variable, so that the energy of the system depends

not only on the displacements in each element, but also explicitly on the size and shape of the unit cell of the system. In response to internal forces that tend to make the material shrink (or expand), the size and shape of the unit cell can then adapt itself so as to minimize the elastic energy and find the correct solution for the overall shrinkage. The internal forces in a porous medium come from the negative pressure in the capillary water, which acts on the solid surfaces with which it is in contact, and the changes in the specific surface energy in the adsorbed water layers.

The effect of the negative pressure in the capillary water is computed by applying the appropriate stress directly to the nodes on the capillary water–solid surface. To handle the effect of the specific surface energy on the system size, a term is added to the system energy of the form

$$U_s = \gamma_s S_A \quad (8)$$

where S_A is the surface area in square metres of the exposed surfaces, and γ_s is the specific surface free energy (J m^{-2}). As before, an exposed surface is a surface that is not covered with capillary water. The surface area of the digital structure can be written in terms of a power series in the displacements of the nodes. Since only small strains are being considered, the series is truncated at linear order. The result is an additional term in the finite-element elastic energy that is linear in the nodal displacements. The system shape and size is then modified to minimize this overall energy. For example, for an unstrained system, with no capillary water, the system will shrink, thereby reducing the surface elastic energy by reducing the surface area at the expense of increasing the volume elastic stored energy by the same amount [8].

An important test case for the treatment of surface energy is that of the dilute limit of a few volume per cent of spherical holes in a solid frame, with a specific surface energy term applied to the surface. This problem is easily solved using spherical polar coordinates [42–44]. One applies a uniform radial displacement U , which would arise due to the application of the surface energy, to the surface of a spherical hole embedded in the centre of a large solid sphere of elastic moduli K_s and G_s . The resulting volume elastic and surface free energy is minimized with respect to U , and the new size of the system computed. For the dilute case, the result for the linear strain ε that arises from the application of the specific surface free energy γ_s is

$$\varepsilon = \frac{-\gamma_s}{6a} \left(\frac{3}{G_s} + \frac{4}{K_s} \right) c \quad (9)$$

where c is the porosity and a is the radius of the hole. In this case, we are starting from $\gamma_s = 0$, so actually $\gamma_s = \Delta\gamma_s$. For a 15 pixel diameter spherical hole in a 40^3 unit cell, the agreement of the finite-element method with the exact result was 4.7%.

Another test case can be found in Scherer's paper [8], the shrinkage per unit surface energy in an intersecting cylinder model. This consists of a simple periodic cubic structure, with equal diameter circular cylinders oriented along the x , y , and z directions, which pass through each other. The radii of the cylinders is a , and the size of the unit cell is L . The quantity $x = a/L$ is determined by the porosity of the model, and the specific surface area is determined by the size of L in real units. Detailed formulae can be found in [8]. A test case was set up using a 60^3 pixel unit cell, with 41 pixel diameter cylinders. The solid had $K_s = 20.44$ GPa, and $G_s = 16.30$ GPa. The theoretical prediction for the shrinkage per unit surface energy was -1.24×10^{-3} , while the finite-element computation gave -1.17×10^{-3} , a difference of only 5.6%.

Mackenzie [6] gives a formula for the dimensional change of a fully-saturated porous medium, which has a pressure p_{cap} in the pore fluid. This equation is only exact when the

solid frame is linearly elastic, and the pores are fully saturated. If K is the bulk modulus of the porous solid, and K_s is the bulk modulus of the material making up the solid frame of the porous solid, then the linear strain ε is given by

$$\varepsilon = \frac{p_{\text{cap}}}{3} \left(\frac{1}{K} - \frac{1}{K_s} \right). \quad (10)$$

The value of K is for empty pores, which assumes that the bulk modulus of the pore fluid has no effect. This will be the case when the bulk modulus of the pore fluid is much less than that of the solid frame, and/or if the pore fluid is free to flow in and out of the porous material as the size of the material changes. For negative pressure (hydrostatic tension), the strain is negative, implying shrinkage. For a partially saturated porous solid, the average of the capillary pressure over the pore space can be used instead of p_{cap} , which brings in a factor of S , the saturation. The resulting *approximate* shrinkage equation for partially saturated porous solids is

$$\varepsilon = \frac{Sp_{\text{cap}}}{3} \left(\frac{1}{K} - \frac{1}{K_s} \right). \quad (11)$$

The shrinkage for the dilute limit of spherical pores filled with a fluid of pressure p_{cap} can be determined from the dilute elastic moduli limit of a spherical hole [45],

$$\frac{K}{K_s} = 1 - \frac{(3K_s + 4G_s)c}{4G_s} \quad (12)$$

where c is the porosity. The finite-element algorithm gives agreement with the exact result to within 1 to 2%. In equation (10), only the effective bulk modulus needs to be known in order to know the strain that arises due to a pressure in all the pores. An analogous result is that of Rosen and Hashin [46] where, for a two-phase random material with arbitrary thermal expansion coefficients and moduli, only the effective bulk modulus needs to be known in order to know the effective thermal expansion coefficient exactly.

We have found that equation (11) holds very well for saturations of 80% or more, but decreases in accuracy for lower saturations. To actually compute the capillary-driven shrinkage for partial saturations, it was necessary to surround the system with a one half pixel thick wall, as shown schematically in 2D in figure 3. Periodic boundary conditions were impossible to accurately maintain without this wall. Without the wall, numerical instability seemed to arise when the system was only partially saturated and periodic boundary conditions were used. The wall was not necessary for computing shrinkage at saturation. The elastic moduli of this wall were chosen so that when the pore space was fully saturated, the exact result according to equation (10) was found. A value of one fifth of the effective moduli of the entire system was used, which was independent of the size of the system in pixels. The choice of the wall moduli compensated for the small increase in surface area caused by the wall touching the pore space, therefore preserving the accuracy of the computational method.

So for both shrinkage mechanisms, negative capillary pressure and changes in specific surface free energy, the finite-element codes give accurate evaluations of exactly known dilute limits, and so should therefore give reasonably trustworthy results for the more complicated porous Vycor glass microstructures. Finite-difference codes were also applied to compute electrical and thermal conductivity, and fluid permeability. The details and accuracy of these algorithms have been described elsewhere [10, 44].

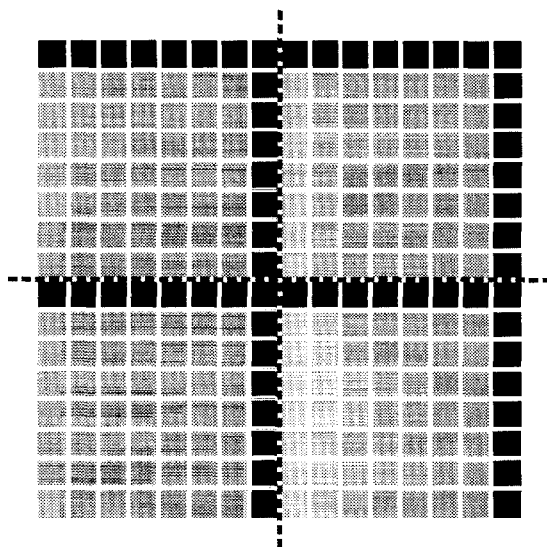


Figure 3. A schematic picture of wall construction (2D) for partially saturated systems. Dashed lines show periodic cell boundaries. Black = wall, grey = material.

3. Microstructure and properties of porous Vycor glass

A two-dimensional binary (pore/solid) image of porous Vycor glass was taken from [15] and [47]. The image provided in the reference was digitized and thresholded, to obtain a binary image with a porosity fraction of 0.31, in agreement with the original measured value [15]. The autocorrelation function measured for this image was then used to reconstruct 3D porous Vycor microstructures with the same porosity, as was discussed earlier. Four different surface area (units of square metres of surface per gram of solid) systems were generated. A $70 \text{ m}^2 \text{ g}^{-1}$ system was generated to compare with the measured surface area of the TEM image, a $100 \text{ m}^2 \text{ g}^{-1}$ system was generated to compare with the actual measured nitrogen BET surface area of this same material, a $129 \text{ m}^2 \text{ g}^{-1}$ system was designed to compare with the material used by Amberg and McIntosh [9] for shrinkage measurements, and a $173 \text{ m}^2 \text{ g}^{-1}$ model was made to match with the material used by Yates for his low RH expansion measurements [5]. Figure 4 shows a slice from each of these four systems, all taken at the same point in the material. The top left is the $70 \text{ m}^2 \text{ g}^{-1}$ model. The surface area then increases clockwise among the four pictures. It is interesting to note that the typical pore size appears to decrease as the surface area increases, with fine scale roughness showing up in the pores for the higher surface area material, reminiscent of what has been referred to as the 'gel' porosity in porous Vycor glass [8].

These generated 3D microstructures were then tested in several ways, in order to check how well their properties compared with real porous Vycor. These computations included: specific surface area, TEM generation, electrical conductivity, thermal conductivity, fluid permeability, elastic moduli, and low (0% RH) and high ($\sim 100\%$ RH) relative humidity shrinkage. In all four systems, the pore space was completely percolated, i.e. there were no isolated pores.

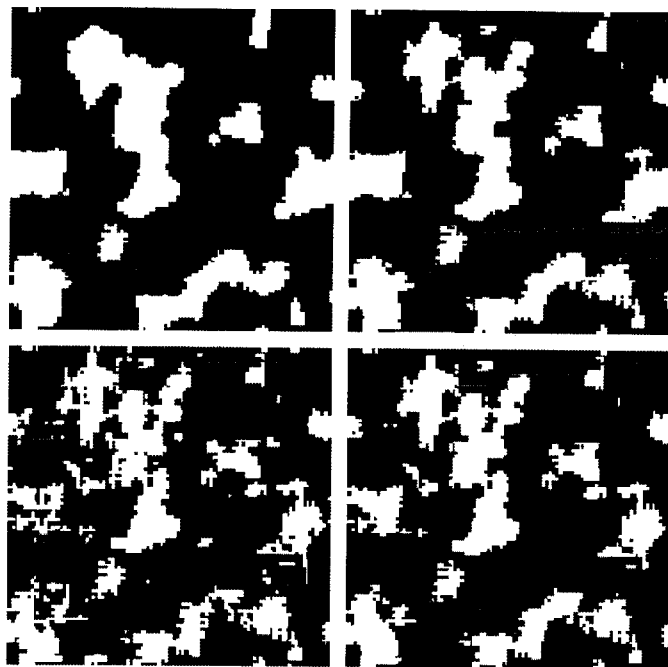


Figure 4. The same slice of different surface area reconstructed porous Vycor glass structures (clockwise from upper left: 70, 100, 129, and 173 m² g⁻¹). Dark grey = solid, white = pore.

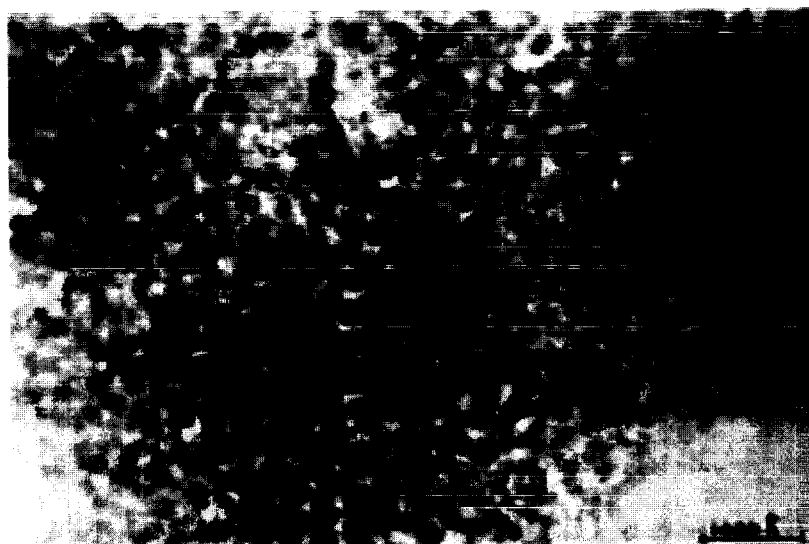
3.1. Surface area

One should note that in computing the surface area of a digital image, there is a correction factor needed. Because the surface area is made up of pixel faces oriented in the x , y , and z directions, the actual surface area is overcounted by a factor of $3/2$. Consider an isolated spherical pore with radius r . Project the pixel faces onto the $\pm x$, $\pm y$, and the $\pm z$ directions. One gets six circles, each with area πr^2 , for a total surface area of $6\pi r^2$, instead of the true surface area of $4\pi r^2$. Therefore, in all cases the digital surface area, computed by counting pixel faces, was corrected downwards by a factor of $2/3$.

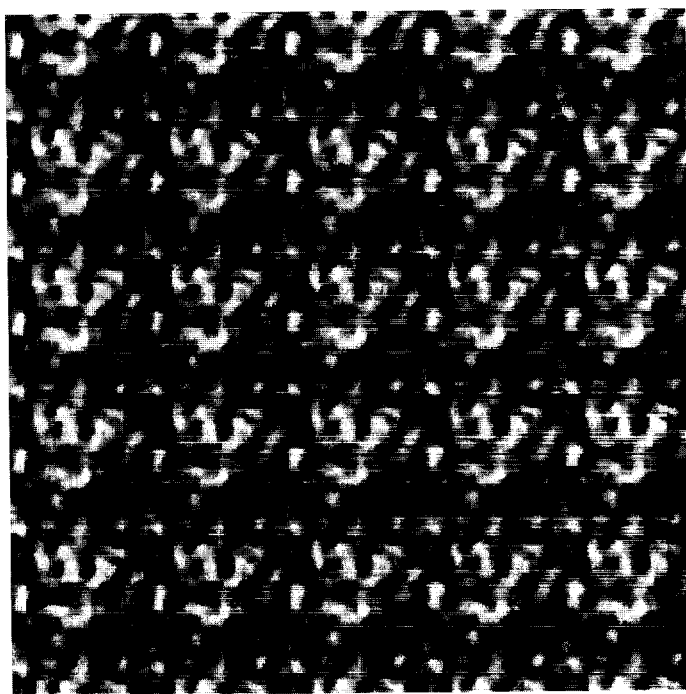
The surface area of the reconstructed system per total volume was computed to be 70 m² g⁻¹ in comparison to the value of 74 m² g⁻¹ computed directly on the 2D image [15]. For this same material, a surface area of 100 m² g⁻¹ was measured using BET analysis of nitrogen sorption [15], which probes the surface structure at a higher resolution than that of the TEM image. The resolution of the TEM image was about 1 nm/pixel, so pores smaller than about 1 nm will be missing from the image, and pores up to a few nanometres in size will be distorted from their original shape, since they will be represented by only a few pixels [48]. These pores will tend to keep water in them down to lower relative humidities. This will cause errors in the model computations of both water sorption and shrinkage [8], as will be discussed further later.

3.2. TEM images

Having a 3D digital model image available makes it simple to approximately simulate the appearance of a TEM micrograph. A slice of the appropriate thickness is taken from the



(a)



(b)

Figure 5. (a) Real and (b) simulated TEM images of reconstructed 3D porous Vycor glass microstructure (40 nm thick, the simulated image is 500 nm by 500 nm). The real image is adapted from [15]. The scale bar on the real image (a) is $1000 \text{ \AA} = 100 \text{ nm}$.

model, and then mapped through the thickness into a 2D image, where the grey level of each pixel in the mapped image depends on the solid density through the thickness of the microstructure at the location of the pixel of interest [1]. Figure 5 shows a comparison between the real (a) and the simulated (b) TEM images. The simulated image has the same surface area as does the experimental TEM image. There is a definite qualitative resemblance between the two images, which, by itself, does not of course tell us very much about the accuracy of the reconstruction algorithm.

3.3. Electrical, thermal, and fluid transport coefficients

Table 1 gives the results of various transport computations on the four systems. Data for a fifth system, listed in the next to the last row of the table, is included for comparison. This model's pore space was made up of three different sizes of randomly placed non-overlapping spherical pores, such that the porosity (0.35) and the surface area ($180 \text{ m}^2 \text{ g}^{-1}$) was similar to the $173 \text{ m}^2 \text{ g}^{-1}$ porous Vycor glass models. The last row of data, for the cylinder model, will be discussed later.

Table 1. Transport and elastic properties for different models.

Model	SA ($\text{m}^2 \text{ g}^{-1}$)	Porosity	F_p	F_s	Permeability 10^{-19} m^2	ν_s	E/E_s	ν
Vycor	70	0.31	16.4	2.06	1.8 ± 0.5	0.1	0.276	0.227
Vycor	100	0.31	16.1	2.12	0.8 ± 0.2	0.1	0.283	0.218
Vycor	129	0.31	15.8	2.18	0.42 ± 0.06	0.1	0.293	0.206
Vycor	173	0.31	16.2	2.24	0.22 ± 0.02	0.1	0.302	0.197
Sphere	180	0.35	∞	2.12	0.0	0.1	0.435	0.143
Cylinder	173	0.32	6.3	1.9	0.57	0.1	0.44 ^a	0.087 ^a

^a In the principal (x, y, z) directions.

Electrical conductivity is examined first. Glass is itself an electrical insulator. If the pores of the porous Vycor were filled with a conductor, however, then the entire sample would be a conductor, since the pore space is percolated. The formation factor F_p is defined as [49] the ratio of the pure conducting (pore) phase conductivity to the bulk sample conductivity, so that F_p is always greater than one. This parameter can be calculated using a finite-element scheme similar to that described for the elastic properties, or a finite-difference scheme [44, 50, 51]. Values of F_p ranging from 15.8 to 16.4 were found for the various surface area porous Vycor models using a finite-difference method. There was very little difference between the x, y , and z directions. An experimental result has been previously obtained for porous Vycor filled with indium metal [52]. A resistivity of $150 \Omega \text{ cm}$ was measured at room temperature, while the room temperature resistivity of pure indium is $8.37 \Omega \text{ cm}$. That gives a formation factor of 17.9, so that the model value is in good agreement with the measured one. Other experimental results by the same authors give $F_p \approx 20$ [53], so there can be some variation from system to system. The experimental papers did not give a measured value of surface area, but as shown above, the value of F_p does not greatly depend on surface area and pore size. The three-sphere model has a disconnected pore space by construction, and so has an infinite value of F_p .

If the pore phase of porous Vycor glass is considered to be empty, then the thermal conductivity of the material will be dominated by heat conduction through the solid phase, with the pore phase now being a thermal insulator. A formation factor F_s can be defined analogously for this case, being defined as the solid backbone thermal conductivity divided

by the porous Vycor thermal conductivity. This can be computed with the same finite-difference method as was the electrical conductivity, with resulting formation factors F_s ranging from 2.06 to 2.24, again with very little difference between the three principal directions. A measured value of the formation factor is $F_s = 2.1$ [54], so again the model prediction agrees well with experiment. As for the pore space conductivity, the value of the thermal conductivity formation factor F_s does not seem to greatly depend on the surface area. The three-sphere model has a value of F_s of 2.12, very close to experiment and to the other model results, so that F_s is not very sensitive to microstructure. If, for instance, the pore phase and the solid phase were arranged in parallel fashion to each other, the value of F_s would be $F_s \approx 1.45$, which is only 31% different from the experimental result.

The electrical conductivity of the pores and the thermal conductivity of the backbone were not very sensitive to pore space details, so are not a stringent test of how well the pore space has been simulated. The permeability, however, should be much more sensitive to pore size, because of the zero velocity boundary condition at all fluid–solid interfaces [50]. The pore space of porous Vycor glass is continuous, so that if the pores are saturated with a fluid, and a pressure gradient is applied, Darcy flow will be observed in the bulk and the fluid permeability can be determined. Using previously developed numerical techniques [50, 55], and neglecting the effect of molecular size, we can compute the fluid permeability, averaged over direction. In table 1, the permeability can be seen to range from $1.8 \times 10^{-19} \text{ m}^2$ for the lowest surface area, and therefore highest hydraulic radius, down to $0.22 \times 10^{-19} \text{ m}^2$ for the highest surface area and therefore lowest hydraulic radius material. The standard deviations listed in the table were computed over the three different principal directions, so that these samples were rather anisotropic as far as permeability was concerned, which is a finite size effect. Experimental values in the literature, using various fluids and techniques, range from 0.4 to $1.0 \times 10^{-19} \text{ m}^2$ [56–58], so in general there is good agreement between the range of model permeabilities and the range of experimental permeabilities. Some of the differences in experimental permeabilities were probably due to molecular size and viscosity differences in the fluids used, but some were on different systems. Unfortunately, none of the references that we found for the permeability of porous Vycor glass also measured the surface area, so we cannot directly compare equivalent experiments and computations. The three-sphere model has zero permeability, because of its disconnected pore space.

For the porous Vycor glass models, clearly the surface area, and therefore the hydraulic radius, is setting the scale for the pore size, since we can think of the permeability as proportional to the inverse of the electrical formation factor times a typical pore size squared [59]. Since the electrical formation factor is roughly constant for the different surface area materials, the typical pore size must be changing with the surface area. If we assume that the typical pore size scales linearly with the surface area [50], then the square root of the permeability ratio should scale as the inverse of the surface area ratio. For the $70 \text{ m}^2 \text{ g}^{-1}$ and $173 \text{ m}^2 \text{ g}^{-1}$ models, the square root of the permeability ratio is 2.9, while the inverse of the surface area ratio is 2.5, so the above statement is approximately true. Comparing the other systems with each other leads to similar results.

3.4. Elastic moduli

The elastic properties of the porous Vycor model were computed using the finite-element code described previously. For a given assignment of bulk and shear moduli for the solid phase, the program computes the porous material moduli with reasonable accuracy. The main question is then: What moduli do we use for the solid backbone? One cannot just use the moduli of fused silica, which is what porous Vycor glass becomes after being fully

sintered. Scherer [8] has shown that the moduli of porous Vycor changes as it is heat treated, even without any changes in the porosity. Apparently this heat treatment drives off hydroxyl groups that tend to soften the solid backbone structure. The solid backbone of as-received porous Vycor glass, therefore, can have a much lower Young's modulus than that of fused silica [8]. The effective Poisson ratio for porous Vycor glass was found to range from 0.15 to 0.19, however, with little change after heat treatment.

Scherer's data can be used to determine the solid backbone moduli to be used in the model in the following way. The porous Vycor glass that Scherer used had a surface area of $149 \text{ m}^2 \text{ g}^{-1}$, so the $173 \text{ m}^2 \text{ g}^{-1}$ model was compared to the experimental results. For heat treatment roughly equivalent to that of Yates [5], Scherer measured a Young's modulus E of 19.6 GPa. The model computation gave $E/E_s = 0.3$, so the solid backbone modulus E_s would be 65 GPa. (The elastic data for all the systems is given in table 1.)

A range of values for ν_s , the Poisson ratio of the solid frame, was chosen, and the effective Poisson ratio, ν , computed. It was found, in agreement with previous work [39], that there was a critical value of ν_s , denoted ν_s^* , such that for $\nu_s < \nu_s^*$, $\nu > \nu_s$, and for $\nu_s > \nu_s^*$, $\nu < \nu_s$. This behaviour is ubiquitous in two-phase materials. It can be shown exactly in two dimensions [60], and has been seen in three dimensions [39, 61], for different kinds of porous microstructures. The particular value of ν_s^* found of course depends on the microstructure. Figure 6 shows the numerical results for the Vycor $173 \text{ m}^2 \text{ g}^{-1}$ model, along with the results of two effective medium theories [62–64] at the same solid volume fraction of 0.69. The effective medium theory curves were added to show that this behaviour is ubiquitous in porous materials [61]. The actual ν against ν_s curves are quite linear, and have a slope less than one. The two effective medium theories have an exact fixed point of $\nu_s^* = 0.2$.

The slope of the ν against ν_s curves will depend on porosity. It is easy to see why this is so. If the porosity were zero, then the ν against ν_s curve would be exactly linear, passing through the origin with a slope of unity, since for any value of ν_s one must have $\nu = \nu_s$. When the porosity becomes non-zero, consider the physically allowed limits for the Poisson ratio of the solid frame, $\nu_s = -1$ and 0.5 [65]. At the $\nu_s = -1$ endpoint, the only way that the porous solid Poisson ratio can change upon introducing porosity is to increase, since ν cannot be less than -1 . At the $\nu_s = 0.5$ endpoint, the porous solid Poisson ratio must decrease when the porosity becomes non-zero, since ν must be less than 0.5. Therefore the ν against ν_s curve goes above the $\nu = \nu_s$ line at negative values of ν , and goes below the $\nu = \nu_s$ line at values of ν_s near 0.5. Somewhere in between the physical limits, the ν against ν_s curve must cross the $\nu = \nu_s$ line, and therefore the behaviour seen here comes about. More analysis of this behaviour is given in [61].

For porous solids made up of randomly placed non-overlapping spherical pores, where the pores are monosize and the porosity ϕ is small, a few per cent at most, one can use the exact dilute limit [44, 45] for spherical pores and directly see how porosity affects the slope of the ν against ν_s curve:

$$\nu = \nu_s + \frac{3(1 - \nu_s^2)(1 - 5\nu_s)\phi}{2(7 - 5\nu_s)}. \quad (13)$$

The value of ν_s^* is clearly 0.2, and $\nu_s < 0.2$, $\nu > \nu_s$, and for $\nu_s > 0.2$, $\nu < \nu_s$. Expanding (13) around $\nu_s^* = 0.2$, one obtains the straight line result $\nu = 0.2 + (1 - 1.2\phi)(\nu_s - 0.2)$, whose slope clearly decreases from one as the porosity increases from zero. The Hashin upper bound for a two-phase material, where one of the phases is porosity [66], also gives this behaviour, where $\nu_s^* = 0.2$ for any porosity.

For the reconstructed Vycor models, ν_s^* was about 0.3, so that in order to achieve a

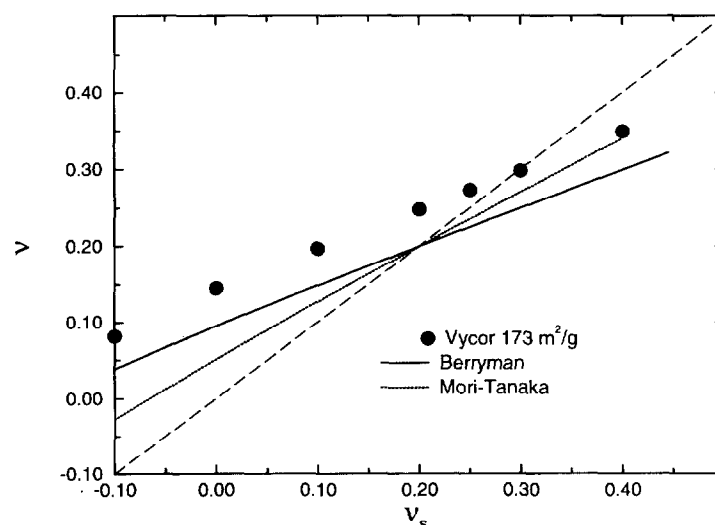


Figure 6. The ν against ν_s curves for the $173 \text{ m}^2 \text{ g}^{-1}$ Vycor model and two effective medium theories [62, 63]. The dashed line is the line of equality, $\nu = \nu_s$.

value of ν between 0.15 and 0.19, the value $\nu_s = 0.1$ was chosen, which gave $\nu = 0.2$. This value of ν_s^* is probably higher than in reality, for the following reason. The elastic moduli of fused quartz, which presumably is what the backbone of Vycor approaches as it is heat treated [8], are $E = 72 \text{ GPa}$ and $\nu_s = 0.16$ [67]. Using $\nu_s = 0.16$ in the $173 \text{ m}^2 \text{ g}^{-1}$ model would give too high a value for ν of the porous solid. If, however, the value of ν_s^* for the $173 \text{ m}^2 \text{ g}^{-1}$ model were lower, say about 0.2 or so, then a backbone value of $\nu_s = 0.16$ would give about the correct value of ν . Looking at figure 6, if the Vycor data points were each lowered by about 0.05, then they would agree closely with the Berryman effective medium theory, and would give a value of ν_s of about 0.2. Also, looking at table 1, one notices that the porous solid Poisson ratio decreases with increasing surface area, or increasing fine structure (see figure 4). Since all of the models are built from the TEM picture, which only has 1 nm resolution, some of the finest Vycor structure is missing from even the $173 \text{ m}^2 \text{ g}^{-1}$ model. If this fine structure could be included in the model, the value of ν obtained would then likely be reduced, in analogy with table 1, and so agree better with the experimental value.

Comparison with the measured Young's modulus of the non-heat-treated porous Vycor glass gave a solid backbone Young's modulus of 49 GPa. To show the effect of microstructure, the next to the last row of table 1 gives elastic data for the non-overlapping spherical pore system previously mentioned. The value of E/E_s is significantly higher, 0.435, and the effective Poisson ratio increases to 0.143 from the backbone value of 0.1, because the value of ν_s^* for this system is 0.22 [61].

For the heat treatment carried out in Yates' work [5], Scherer [8] estimated that the backbone Young's modulus would be about $E_s = 50 \text{ GPa}$. For Amberg's material, which was not heat treated, the backbone Young's modulus was estimated to be about $E_s = 38 \text{ GPa}$. The cylinder model mentioned previously was used to determine these values. However, this model is anisotropic, since it is inherently cubic. There are therefore three independent elastic moduli, C_{11} , C_{12} , and C_{44} , not just a Young's modulus and Poisson ratio, as reported by Scherer [68, 69]. Scherer predicted the Young's modulus and Poisson ratio in the

three principal directions, which are not the same as those determined by carrying out an isotropic average of the elastic moduli tensor. Because this cubic model is stiffer in the three principal directions, along the cylinders, the Young's modulus of the porous Vycor glass is overestimated by this model. Table 1 shows that $E/E_s = 0.44$ for this model, in the principal directions and at a porosity of 0.32, in good agreement with the approximate analytic value predicted [8] but significantly stiffer than the reconstructed model. That is why the backbone modulus predictions of Scherer [8] are smaller than in the present work. Also, the Poisson ratio in any of the three principal directions for the cylinder model is predicted to always be smaller than the solid backbone Poisson ratio [8] (which checks with computed results). This is not the case for an isotropic single solid phase material [61], for the reasons given above. Rather, one would expect a critical value of ν_s , as has been demonstrated for the reconstructed models and for other microstructures [39, 60, 61].

3.5. Low relative humidity shrinkage

At very low relative humidities, where the material has no capillary condensed water, length change (shrinkage on desorption and expansion on adsorption) depends only on changes in the specific surface energy of the adsorbed water layer. Comparison to experiment in this regime then does not depend on details of the absorption/desorption algorithm, but only on the elastic properties and surface area of the model.

Yates [5] has published data on the expansion due to the adsorption of various gases on the pore surfaces in porous Vycor. Based on Scherer's analysis [8] of this data, for argon, below capillary condensation, the expansion strain could be expressed as $0.00545 \text{ (m}^2 \text{ J}^{-1}) \Delta\gamma$. In other words, a change of 1 J m^{-2} in the specific surface energy would produce a strain of 0.00545, taking totally dry Vycor as the baseline of zero strain. Amberg and McIntosh [9] have made the same measurement for the adsorption of water vapour. The strain coefficient was found to be about $0.01 \text{ (m}^2 \text{ J}^{-1})$ [8]. Hiller, for water absorption in a similar material, also found a strain coefficient of about $0.01 \text{ (m}^2 \text{ J}^{-1})$ [70]. The porous Vycor glass used by Amberg and McIntosh had a lower surface area than Yates, 129 against $173 \text{ m}^2 \text{ g}^{-1}$, which would tend to decrease the strain slope. However, the glass used by Amberg and McIntosh was not heat treated, so it would have had a lower backbone modulus. These two effects roughly cancel out, so that both glasses should have had approximately the same strain slope [8]. This relative increase for water vapour against argon was attributed by Scherer [8] to the *absorption* of water into the glass backbone, due to the many hydroxyl groups present in the glass before heat treatment at 500°C , which causes swelling of the solid backbone, and hence swelling of the porous composite. Since this mechanism is not present in our computations, we will compare our results to Yates' value of $0.00545 \text{ (m}^2 \text{ J}^{-1}) \Delta\gamma$, or a strain coefficient of 0.00545. The measured nitrogen BET surface area of Yates material was $173 \text{ m}^2 \text{ g}^{-1}$, so this reconstructed model was used for computing the surface energy-driven expansion/shrinkage. For the $173 \text{ m}^2 \text{ g}^{-1}$ model, a backbone value of $E_s = 59.1 \text{ GPa}$, with $\nu_s = 0.1$, gives a strain coefficient of -5.45×10^{-3} , in exact agreement with experiment and with Scherer's prediction. The surface energy-driven shrinkage of the cylinder model also agrees well with experiment, using the lower values for the backbone modulus [8]. Scherer's prediction, with his values of the backbone modulus, also agrees well with the model prediction, when $E_s = 44.9 \text{ GPa}$, for the strain coefficient of the $129 \text{ m}^2 \text{ g}^{-1}$ material: 5.4×10^{-3} (Scherer) against 5.2×10^{-3} (model).

3.6. High relative humidity shrinkage

Another limit that can be critically examined is the high relative humidity limit. In this limit, as the RH value decreases from 1, the sample stays essentially fully saturated, but the water is placed under a negative pressure (hydrostatic tension). Therefore, Mackenzie's formula, equation (10), applies, and is exact. Amberg and McIntosh have data for 94% and 82% RH, at which, according to the model and experiment (see figure 7), the pores are still filled. The experimental shrinkage strain increase between these two RH values is 0.000 530. Using Mackenzie's formula applied to the model, with $E_s = 40.8$ GPa and $\nu_s = 0.1$, makes the model agree perfectly with the experimental value.

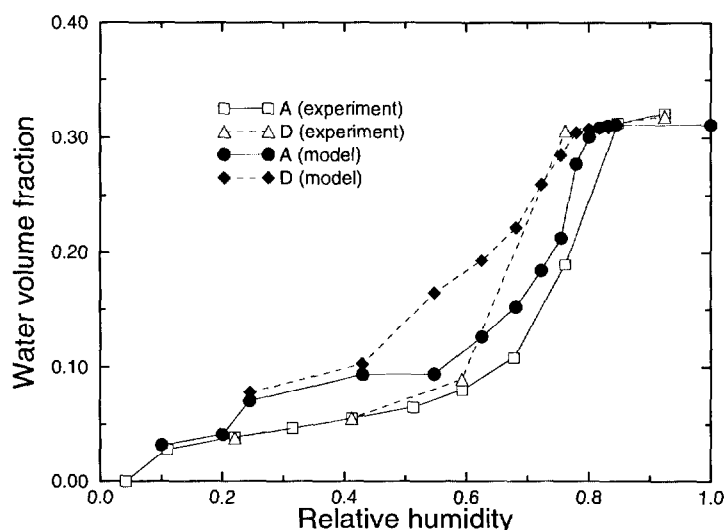


Figure 7. Simulated ($129 \text{ m}^2 \text{ g}^{-1}$) and experimental sorption curves for the porous Vycor glass (A = adsorption, D = desorption).

3.7. Best values of backbone Young's modulus

Using these three experimental data points, the measured elastic moduli and the low and high RH shrinkage measurements, one can obtain a value for the backbone Young's modulus that makes the model agree well with these experiments. For the $129 \text{ m}^2 \text{ g}^{-1}$, non-heat-treated model, the elastic moduli imply $E_s = 49$ GPa, while the high relative humidity shrinkage measurement implies that $E_s = 40.8$ GPa. We then take their average, 44.9 GPa, which gives an accuracy of -8.4% in the modulus and 10% with respect to the high relative humidity data point. For the $173 \text{ m}^2 \text{ g}^{-1}$ model, a value of $E_s = 65$ GPa is necessary for agreement with the elastic modulus, while a value of $E_s = 59.1$ GPa is implied by the low RH strain slope. Therefore, a value of 62 GPa is used, the average of these two values, which gives an error of -4.6% in modulus and 4.9% in the strain coefficient. The Young's modulus ratio for porous Vycor glass, between the non-heat-treated and heat-treated $173 \text{ m}^2 \text{ g}^{-1}$ models, according to these choices of backbone moduli, is then 1.42, which is in good agreement with the measured ratio of moduli, $19.6/14.7 = 1.33$ for a $149 \text{ m}^2 \text{ g}^{-1}$ system of similar porosity [8].

To infer solid backbone moduli from measured porous material moduli requires, in most cases, a model of how the pores affect the measured moduli. The above choices are the best

for our reconstructed models. There is no reason to prefer the values of backbone moduli inferred in [8], since the cylinder model used was not isotropic. Its success in predicting the low RH strain coefficient was probably due to the fact that the backbone moduli were picked so that the composite, effective moduli were the same as experiment. Also, the shrinkage strain tensor is second order, and so it is isotropic even for a cubic system like the cylinder model.

4. Water sorption and shrinkage results

Figure 7 provides a comparison between the water sorption curves determined using the spherical interface approximation on the $129 \text{ m}^2 \text{ g}^{-1}$ reconstructed model, and those measured experimentally. The surface area of the experimental system was not characterized, which may certainly lead to some disagreement between model and experimental results. Also, there is no temperature in the model algorithm, which could also lead to some disagreement with experiment, since the shape of the hysteresis loop in adsorption-desorption isotherms does depend on temperature [33]. The hysteresis in the model results is entirely from pore network percolation effects, and so is independent of temperature.

For desorption, the agreement between model and experimental results appears to be reasonably good down to about 80% RH. After that point, the model appears to retain more water than does the experiment. However, there is no experimental data between 75% and 60% RH. The breakthrough point could be as far down as 70%, which would give a region where the model has less water than experiment (between 70 and 75% RH), followed by a region where the model retains more water than experiment (20 to 70% RH).

For adsorption, starting at low RH, the agreement with experiment is good up to about 20% RH, and for RH values larger than 80%. Below 20% RH, the amount of water retained is determined by the thickness of the adsorbed film and the surface area of the material. It appears that these match well between model and experiment. At intermediate humidities, the model picks up capillary water steadily, while the amount of water in the experimental curve stays low and then rises rapidly at about 60% RH. By differentiating the desorption isotherm, an estimated pore size distribution can be obtained. For the simulation and experimental data, a fairly broad peak with a peak value at a pore radius of about 3–5 nm was obtained. This value agrees fairly well with the values of 3.5 nm measured experimentally by Levitz *et al* [15] using nitrogen sorption and 5.7 nm measured by Scherer [8] using nitrogen sorption.

The model results in figure 7 were obtained using a 200^3 digital image model. It is probable that using a higher resolution system would improve results, but by how much we do not know, as the available computer power is not adequate to go much higher in resolution. In some respects, there is little point in going much higher in resolution, as we are limited by the experimental resolution of the original TEM image, which is about 1 nm/pixel. However, the adsorption-desorption algorithm uses digitized spheres in order to find the location of capillary-condensed water. The diameter of these spheres goes down to three pixels, since each pixel is a nanometre in length. A sphere that is three pixels in diameter does not look terribly spherical. Having more resolution available at these small diameters, or more pixels per nanometre, would allow better spherical shapes to be used to compute the location of capillary-condensed water at intermediate RH values. Also, the true shape of pores that are 1–5 nm in size would also be resolved better if there were more than one pixel per nanometre. Both these effects might improve results in the intermediate RH regime.

Since the surface area of the experimental sample was not measured, there could also be some differences between model and experiment due to different surface areas. However, at low RH, as was mentioned above, the model agrees quite well with experiment. In this regime, the water content is approximately just the surface area times the water layer thickness, so the experimental surface area was probably similar to that of the model, $129 \text{ m}^2 \text{ g}^{-1}$, assuming of course that the layer thickness used was also accurate.

The known inaccuracy of the Kelvin–Laplace equation at small pore diameters (5–10 nm) would certainly seem to contribute to the differences between model and experiment in the intermediate RH regime. However, the hysteresis loop in the adsorption–desorption isotherms, which makes up the intermediate RH regime, may result mostly from pore network percolation effects [30,33]. In fact, untangling single-pore adsorption–desorption effects from pore network effects is a difficult question [30]. So it is impossible, with any degree of certainty, to determine how much of the disagreement between model and experiment in the intermediate RH regime is due to the inaccuracy of the Kelvin–Laplace equation for small pores. It is also known that the percolation aspects of reconstructed microstructures can differ from the real microstructures [10]. This is because 2D images have no 3D percolation information in them, so that this information, in contrast to quantities like surface area and porosity, is put in entirely by the reconstruction process. Since hysteresis is sensitive to the pore space percolation, there will also be some error in the intermediate RH regime arising from this cause. For globally averaged quantities like electrical and thermal conductivity, fluid permeability, and elastic moduli, the model microstructure gave values close to experiment. A more local quantity, such as how much water is capillary condensed at a given relative humidity, is clearly much more sensitive to the details of the pore space.

Figure 8 shows four partially-saturated slices of the $129 \text{ m}^2 \text{ g}^{-1}$ model, all taken at the same position, but at different RH values, starting with $\text{RH} = 0.494$ in the upper left, then going clockwise to higher RH values ($\text{RH} = 0.494, 0.656, 0.740, 0.791$). The slices were taken from systems undergoing adsorption. White is capillary-condensed water, grey is empty pore space, and black is solid material. It is clear that water is added first to the smaller pores, and then to progressively larger pores as the relative humidity is increased. In 3D, using the adsorption algorithm described earlier, the menisci are roughly spherical, so their 2D cross sections are roughly circular.

Figure 9 provides a plot of the computed shrinkage at general relative humidities, showing the experimental data of Amberg and McIntosh [9] for a $129 \text{ m}^2 \text{ g}^{-1}$, non-heat-treated system. All results have been normalized to have zero shrinkage at 94% relative humidity, the maximum humidity for which experimental results were recorded [9]. At partial and full saturations, the surface energy was only put on the part of the solid backbone that was free from capillary-condensed water, since this term goes to zero for a thick capillary-condensed water layer. Very good agreement is demonstrated between model computation and experimental measurement from 94% RH down to about 80% RH. After that, the experimental values stay higher than those from the model. Since the model, as can be seen in figure 7, retains more water than does the experimental desorption at intermediate relative humidities, it would seem that the model values should go above the experimental values, not below. We attribute this to the same phenomenon that gives a higher strain coefficient at low RH, that of water absorption into the solid backbone and thus swelling of the backbone. As water leaves the pore space it leaves areas of the backbone dry and able to lose water into the empty pore space. This will cause more shrinkage than what is due to capillary forces alone, and ultimately result in a higher, by about a factor of two, strain coefficient at low RH.

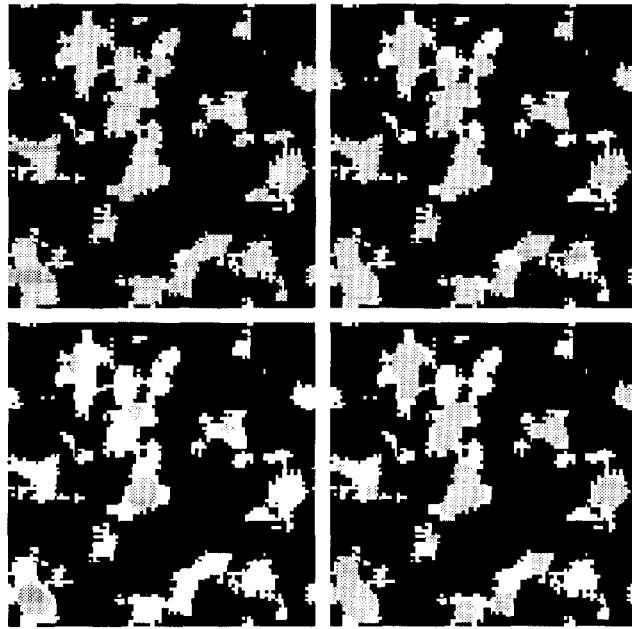


Figure 8. Same slices of $129 \text{ m}^2 \text{ g}^{-1}$ model showing partially saturated conditions at different relative humidities (clockwise from upper left: $\text{RH} = 0.494, 0.656, 0.740$, and 0.791) during adsorption. Black = solid, light grey = empty pore, white = liquid water.

Shrinkage: Experiment and Analytical

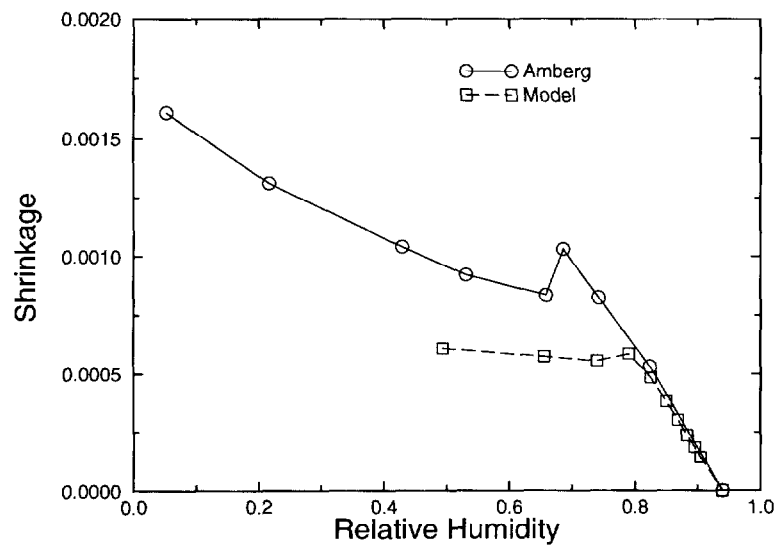


Figure 9. Experimental and model shrinkage for porous Vycor glass ($129 \text{ m}^2 \text{ g}^{-1}$) as a function of relative humidity.

The results of the model do tend to confirm a previously proposed explanation [9] for the observation of a local maximum in the shrinkage against relative humidity curves for porous Vycor. Basically, capillary-induced stresses are being replaced by stresses of a smaller magnitude caused by changes in the specific surface energy. Depending on the relative humidity at which the majority of the capillary pores empty, the new surface energy stresses may or may not exceed the lost capillary-induced stresses. As shown in figure 2, the surface energy contribution will be much larger if the pores empty at a low RH (<50%) than if they empty at a higher one (> 60% as in this study), since the specific surface energy is higher at lower RH values. Thus, the observation of a local maximum in the shrinkage curves will depend on the pore structure of the material as well as on its surface energy characteristics. The model also clearly indicates how strongly capillary-induced shrinkage is dependent on the amount of capillary water in the microstructure, implying that sorption isotherms are critical measurements for characterizing the shrinkage behaviour of porous materials.

5. Discussion

A general pore space cannot accurately be thought of as pores with a certain shape that are linked up like tubes in a network [34,71]. The finite-element techniques discussed in this paper for computing shrinkage, along with the algorithm for estimating the location of capillary-condensed water at a given RH value [1], constitute a novel technique for modelling moisture-induced volume changes, including drying shrinkage, of porous materials with general pore shapes and pore network topology. The technique for locating capillary-condensed water is only approximate, however, because the Kelvin–Laplace equation becomes inaccurate for very small pore sizes, and because the spherical interface approach has only one radius of curvature, whereas real menisci have, in 3D, two radii of curvature.

Techniques were previously developed to produce a reconstructed 3D representation of the porous medium from a 2D micrograph. In this paper, this reconstruction technique has been applied to porous Vycor glass, giving a 3D pore structure upon which the shrinkage algorithm has been demonstrated and the reconstruction algorithm checked. Computed properties such as elastic moduli, fluid permeability, and electrical and thermal conductivity, have been used for comparison with experimental measurements, in order to test how close the reconstructed model comes to reality.

The thermal conductivity of the backbone agreed well with experiment. However, this quantity is not very sensitive to microstructure, because the three-sphere model gave results close to that of the porous Vycor models, and these all had similar results, even though their surface areas were very different. The formation factor of the pore space was also nearly invariant with surface area, and agreed well with experiment. Even though these quantities are not very sensitive to microstructure, and cannot be used by themselves as a check on a model, it does seem true that if a model cannot reproduce these quantities in agreement with experiment, then there is something lacking in the model's representation of the microstructure. Taking the cylinder model with a ratio of cylinder radius to unit cell size of $x = 0.355$ gives a model with a porosity of 0.32. While the computed solid thermal formation factor is reasonable, 1.9, the pore space formation factor is only 6.3, three times less than the experimental measurements. The cylinder model is isotropic with respect to conductivity, as the conductivity is a second rank tensor. Based on this result alone, the microstructure of this model does not reproduce the porous Vycor microstructure as well as does the reconstructed models. However, the cylinder model has only a single

pore size, compared to the distribution of pore sizes available in the reconstructed models. Because of this fact, one might not expect it to describe Vycor as well as the reconstructed models.

The fluid permeabilities were really a test of pore size, since the tortuosity of the pore space was in a sense given by the reciprocal of the pore space formation factors. Reasonable agreement with experimental results were obtained, although experimental and model results could not be precisely matched because the surface area of the samples used in the experiments was not measured. If the length scale of the cylinder model is chosen so that the cylinder radius is 3.33 nm at $x = 0.355$, with $L = 9.4$ nm, the cylinder model then has $173 \text{ m}^2 \text{ g}^{-1}$ of surface area. The permeability can easily be computed using the same techniques, and is found to be $0.57 \times 10^{-19} \text{ m}^2$ along one of the principal directions, in reasonable agreement with the range of experimental and model values found. However, the square opening between the cylinders along one of the principal directions then has width $L - 2a = 2.7$ nm. This size opening seems small, compared to experimental pore diameters of about 7–11 nm [8, 15]. This combination of a too small 'pore width' and a too large value of $1/F$ for the pore space combine to give a reasonable permeability along one of the principal directions. Since the Darcy permeability tensor is second rank, the cylinder model will have an isotropic permeability tensor. However, if we assume that the cylinder model represents only the main skeleton of Vycor, and not the very fine pores of the 'gel' [8], a better value of surface area might be $100 \text{ m}^2 \text{ g}^{-1}$, as about one third of the surface area of Vycor is in the very smallest pores [8]. In this case, we get an opening of about 5 nm in diameter, which is in better agreement with experimental measurements of the principal pore size in Vycor [8, 15].

The backbone elastic moduli of the reconstructed systems were chosen by fitting to either the measured elastic moduli, the low RH shrinkage, or the high RH shrinkage. The backbone moduli that came from these experiments agreed well with each other, giving additional validity to this process. The model, therefore, did a good job of predicting these three quantities using an average backbone Young's modulus. However, the actual value of ν_s^* for Vycor is probably about 0.2, while the model gave a value of about 0.3. This implies that there is a subtle difference in microstructure between real Vycor and the model that causes this disagreement. The reasons that a microstructure has a certain value of ν_s^* is a subject of further research [61].

At intermediate RH values, the amount of water retained by the model was more than in experiment, causing some error in shrinkage prediction. However, the phenomenon of water swelling of the solid backbone may have caused most of the disagreement in shrinkage strain at intermediate humidities (see figure 9), since the additional water in the model would tend to make the model shrinkage greater than the experimental value, not less. This phenomenon certainly made the experimental low RH shrinkage higher than was predicted, as the argon results on the $173 \text{ m}^2 \text{ g}^{-1}$ system [5] were very well predicted, and there was no reason to believe that these results for the $129 \text{ m}^2 \text{ g}^{-1}$ material used by Amberg and McIntosh [9] would not be equally well predicted.

Properties such as the solid thermal conductivity, the pore space conductivity, and the high RH shrinkage strain are mainly functions of porosity only, and are not very sensitive to pore surface area. However, some of the properties of porous Vycor glass are sensitive to the surface area, namely fluid permeability, low RH shrinkage, and water adsorption and desorption. One difficulty then in comparing model results to experimental results was that in many cases the surface area of the porous Vycor glass was not measured. The other difficulty was that water was used as the fluid for the desorption–adsorption measurements, which brought in the solid backbone water-swelling effect, which was beyond

the scope of our model. In areas that were comparable, however, the model compared well to experimental results. In light of this good comparison with porous Vycor glass, we feel that the reconstruction method offers a reasonable method for obtaining accurate 3D models of porous materials from 2D images.

Finally, in the future we feel that it would be very interesting if experimental measurements of the kind described in this paper (both kinds of formation factor, fluid permeability, elastic moduli, adsorption–desorption, and shrinkage) were all made on a single kind of porous Vycor glass, with a measured surface area, and using a gas like argon for the adsorption–desorption measurements, so that the effect of swelling of the solid backbone was not present. Then a complete comparison could be made with model predictions. Based on the results in this paper, we feel that the reconstructed models would continue to do quite well in such a more rigorous comparison.

Acknowledgments

Dale Bentz would like to thank the Centre International des Etudiants et Stagiaires (CIES) for a grant which allowed this research to be initiated during a six-month stay at the Centre Scientifique et Technique du Batiment (CSTB) in Saint-Martin d'Herès, France. We thank H Sallée of CSTB for measuring the experimental sorption isotherms for the porous Vycor glass presented in figure 7. We would also like to thank G W Scherer and W Haller for critically reading the manuscript, for useful conversations about the microstructure and properties of porous Vycor, and for supplying important references. Finally, we thank P Levitz for permission to reproduce the real TEM image of porous Vycor shown in figure 5(a).

References

- [1] Bentz D P, Quenard D A, Baroghel-Bouny V, Garboczi E J and Jennings H M 1995 Modelling drying shrinkage of cement paste and mortar: Part I. Structural models from nanometers to millimeters *Mater. Struct.* **28** 450–58
- [2] Carino N J and Clifton J R 1995 Prediction of cracking in reinforced concrete structures *NISTIR* 5634, US Department of Commerce, April
- [3] Scherer G W 1990 The theory of drying *J. Am. Ceram. Soc.* **73** 3–14
- [4] Flood E A and Heyding R D 1954 Stresses and strains in adsorbent–adsorbate systems *Can. J. Chem.* **32** 660–82
- [5] Yates D J C 1954 The expansion of porous glass on the adsorption of non-polar gases *Proc. R. Soc. A* **224** 526–44
- [6] Mackenzie J K 1950 The elastic constants of a solid containing spherical holes *Proc. Phys. Soc.* **683** 2–11
- [7] Biot M A 1941 General theory of three-dimensional consolidation *J. Appl. Phys.* **12** 155–64
- [8] Johnson D L 1982 Elastodynamics of gels *J. Chem. Phys.* **77** 1531–9
- [9] Scherer G W 1986 Dilatation of porous glass *J. Am. Ceram. Soc.* **69** 473–80
- [9] Amberg C H and McIntosh R 1952 A study of absorption hysteresis by means of length changes of a rod of porous glass *Can. J. Chem.* **30** 1012–32
- [10] Bentz D P and Martys N S 1995 Hydraulic radius and transport in reconstructed model three-dimensional porous media *Transport Porous Media* **17** 221–38
- [11] Crossley P A, Schwartz L M and Bavanar J R 1991 Image-based models of porous media: application to Vycor glass and carbonate rocks *Appl. Phys. Lett.* **59** 3553–5
- [12] Cahn J W 1965 Phase separation by spinoidal decomposition in isotropic systems *J. Chem. Phys.* **45** 93
- [13] Haller W 1965 Rearrangement kinetics of the liquid–liquid immiscible microphases in alkali borosilicate melts *J. Chem. Phys.* **42** 686–93
- [14] Monette L, Grest G S and Anderson M P 1994 Three-dimensional Ising system with long-range interactions: a computer model of Vycor glass *Phys. Rev. E* **50** 3361–9

- [15] Levitz P, Ehret G, Sinha S K and Drake J M 1991 Porous Vycor glass: the microstructure as probed by electron microscopy, direct energy transfer, small-angle scattering, and molecular adsorption *J. Chem. Phys.* **95** 6151–61
- [16] Berryman J G 1985 Measurement of spatial correlation functions using image processing techniques *J. Appl. Phys.* **57** 2374–84
- [17] Cressie N 1991 *Statistics for Spatial Data* (New York: Wiley) ch 2
- [18] Quiblier J A 1984 A new three-dimensional modeling technique for studying porous media *J. Coll. Interface Sci.* **98** 84–102
- [19] Pimentia P J P, Carter W C and Garboczi E J 1992 Cellular automaton algorithm for surface mass transport due to curvature gradients: simulations of sintering *Comput. Mater. Sci.* **1** 630–7
- [20] Bentz D P, Pimentia P J P, Garboczi E J and Carter W C 1992 Cellular automaton simulations of surface mass transport due to curvature gradients: simulations of sintering in 3D *Synthesis and Processing of Ceramics (Mater. Res. Soc. Proc. 249)* ed W E Rhine, T M Shaw, R J Gottschall and Y Chen (Pittsburgh, PA: Materials Research Society) pp 413–8
- [21] Bullard J W, Garboczi E J, Carter W C and Fuller E R 1995 Numerical methods for computing interfacial mean curvature *Comput. Mater. Sci.* **4** 1–14
- [22] Garboczi E J and Bentz D P 1991 Digitized simulation of mercury intrusion porosimetry *Ceram. Trans.* **16** 365–80
- [23] Quenard D A, Bentz D P and Garboczi E J 1992 Capillary condensation, hysteresis, and image analysis *Proc. Int. Drying Symp.* ed A S Mudjundar (Amsterdam: Elsevier) pp 253–62
- [24] Lewis J A, Galler M A and Bentz D P 1996 Computer simulation of binder removal from 2D and 3D model particulate bodies *J. Am. Ceram. Soc.* **79** 1377–88
- [25] Badmann R, Stockhausen N and Setzer M J 1981 The statistical thickness and the chemical potential of adsorbed water films *J. Coll. Interface Sci.* **82** 534–42
- [26] Hagymassy J Jr, Brunauer S and Mikhail R Sh 1969 Pore structure analysis by water vapour adsorption *J. Coll. Interface Sci.* **29** 485–91
- [27] Sneek T and Oinonen H 1970 Measurements of pore size distribution of porous materials *Julkaisu 155 Publication State Inst. Techn. Res., Helsinki, Finland*
- [28] Peterson B K and Gubbins K E 1987 Phase transitions in a cylindrical pore: grand canonical Monte Carlo, mean field theory, and the Kelvin equation *Mol. Phys.* **62** 215–26
- [29] Lastoskie C, Gubbins K E and Quirke N 1993 Pore size distribution analysis of microporous carbons: a density function approach *J. Phys. Chem.* **97** 4786–96
- [30] Evans R 1990 Fluids adsorbed in narrow pores: phase equilibria and structure *J. Phys.: Condens. Matter* **2** 8989–9007
- [31] Tarazona P, Marconi U and Evans R 1987 Phase equilibria of fluid interfaces and confined fluids: non-local versus local density functionals *Mol. Phys.* **60** 573–95
- [32] Evans R 1990 *Liquids at Interfaces (Les Houches Session XLVIII)* ed J Charvolin, J Joanny and J Zinn-Justin (Amsterdam: Elsevier)
- [33] Ball P C and Evans R 1989 Temperature dependence of gas adsorption on a mesoporous solid: capillary criticality and hysteresis *Langmuir* **5** 714–23
- [34] Seaton N A 1991 Determination of the connectivity of porous solids from nitrogen sorption measurements *Chem. Eng. Sci.* **46** 1895–909
- [35] Sallée H, Quenard D A and Laurent J P 1993 Développement d'un analyseur hygrogravimétrique automatique pour produit hygroscopique *Récents Progrès en Génie des Procédés, Conduite et Commande des Procédés-Grenoble 93* vol 7 (Lavoisier Technique et Documentation) pp 263–8
- [36] Bangham D H and Fakhoury N 1930 The swelling of charcoal I *Proc. R. Soc. A* **130** 81
Bangham D H, Fakhoury N and Mohamed A F 1932 The swelling of charcoal II *Proc. R. Soc. A* **138** 162
Bangham D H and Fakhoury N 1934 The swelling of charcoal III *Proc. R. Soc. A* **147** 152
Bangham D H and Fakhoury N 1934 The swelling of charcoal IV *Proc. R. Soc. A* **147** 175
- [37] Hansen W 1987 Drying shrinkage mechanisms in Portland cement paste *J. Am. Ceram. Soc.* **70** 323–8
- [38] Iler R K 1979 *The Chemistry of Silica* (New York: Wiley) pp 645–7
- [39] Garboczi E J and Day A R 1995 An algorithm for computing the effective linear elastic properties of heterogeneous materials: 3D results for composites with equal phase Poisson ratios *J. Mech. Phys. Solids* **43** 1349–62
- [40] Cook R D, Malkus D S and Plesha M E 1989 *Concepts and Applications of Finite Element Analysis* (New York: Wiley)
- [41] Torquato S 1991 Random heterogeneous media: microstructure and improved bounds on effective properties *Appl. Mech. Rev.* **44** 37–76

- [42] Neubauer C M, Jennings H M and Garboczi E J 1996 A three-phase model of the elastic and shrinkage properties of mortar *J. Adv. Cem.-Based Mater.* **4** 6–20
- [43] Garboczi E J and Bentz D P 1997 Analytical formulas for interfacial transition zone properties *J. Adv. Cem.-Based Mater.* **6** 99–108
- [44] Garboczi E J 1998 Finite element and difference codes for computing the linear electrical and elastic properties of digital images of random materials *National Institute of Standards and Technology Internal Report* in review (see chapter 2 of <http://ciks.cbt.nist.gov/garboczi/>)
- [45] Christensen R M 1991 *Mechanics of Composite Materials* (Malabar, FL: Krieger) ch 2
- [46] Rosen B W and Hashin Z 1970 Effective thermal expansion coefficients and specific heats of composite materials *Int. J. Engn. Sci.* **8** 157–73
- [47] Levitz P and Tchoubar D 1992 Disordered porous solids: from chord distribution to small angle scattering *J. Physique* **2** 771–90
- [48] Garboczi E J, Thorpe M F, DeVries M and Day A R 1991 Universal conductivity curve for a plane containing random holes *Phys. Rev. A* **43** 6473–82
- [49] Roberts J N and Schwartz L M 1985 *Phys. Rev. B* **31** 5990–6000
- [50] Martys N and Garboczi E J 1992 Length scales relating the fluid permeability and electrical conductivity in random two-dimensional model porous media *Phys. Rev. B* **46** 6080–90
- [51] Garboczi E J and Bentz D P 1992 Computer simulation of the diffusivity of cement-based materials *J. Mater. Sci.* **27** 2083–92
- [52] Graf M J, Huber C A, Huber T E and Salzberg A P Indium-impregnated porous glass: magnetotransport and superconducting transition *Physical Phenomena in Granular Materials (MRS Proc. 195)* ed G D Cody, T H Geballe and P Sheng (Pittsburgh, PA: Materials Research Society) pp 397–402
- [53] Graf M J, Huber T E and Huber C A 1992 Superconducting properties of indium in the restricted geometry of porous Vycor glass *Phys. Rev. B* **45** 3133–6
- [54] Cahill D G, Stephens R B, Tait R H, Watson S K and Pohl R O 1990 *Proc. 21st Int. Thermal Conductivity Conf.* (New York: Plenum) p 3
- [55] Schwartz L M, Martys N, Bentz D P, Garboczi E J and Torquato S 1993 Cross property relations and permeability estimation in model porous media *Phys. Rev. E* **48** 4584–91
- [56] Debye P and Cleland R L 1959 Flow of liquid hydrocarbons in porous Vycor *J. Appl. Phys.* **30** 843–9
- [57] Lin M Y, Abeles B, Huang J S, Stasiewski H E and Zhang Q 1992 Viscous flow and diffusion of liquids in microporous glasses *Phys. Rev. B* **46** 10 701–5
- [58] Nordberg M E 1944 Properties of some Vycor-brand glasses *J. Am. Ceram. Soc.* **27** 299–305
- [59] Katz A J and Thompson A H 1987 *Phys. Rev. B* **34** 8179–82
- Katz A J and Thompson A H 1987 *J. Geophys. Res.* **92** 599
- Thompson A H, Katz A J and Krohn C E 1987 *Adv. Phys.* **36** 625
- [60] Day A R, Snyder K A, Garboczi E J and Thorpe M F 1992 The elastic moduli of a sheet containing circular holes *J. Mech. Phys. Solids* **40** 1031–51
- [61] Garboczi E J 1998 Poisson's ratio and surface-energy-driven expansion of linear elastic porous materials *J. Mech. Phys. Solids* in preparation
- [62] Berryman J G 1980 *J. Acoust. Soc. Am.* **68** 1809–19
- [63] Zimmerman R W 1995 Behavior of the Poisson ratio of a two-phase composite material in the high-concentration limit *Appl. Mech. Rev.* **47** S38–44
- [64] Mori T and Tanaka K 1973 Average stress in matrix and average elastic energy of materials with misfitting inclusions *Acta. Metall.* **21** 571–4
- [65] Landau L D and Lifshitz E M 1986 *Theory of Elasticity* (Oxford: Pergamon) p 12
- [66] Hashin Z 1983 Analysis of composite materials: a survey *J. Appl. Mech.* **50** 481–505
- [67] Weast R C (ed) 1976 *CRC Handbook of Chemistry and Physics* (Cleveland: CRC Press) p F-80
- [68] Scherer G W 1979 Sintering inhomogeneous glasses: application to optical waveguides *J. Non-Crystal Solids* **34** 239–56
- [69] Scherer G W and Drexhage M G 1985 Stress in leached phase-separated glass *J. Am. Ceram. Soc.* **68** 419–26
- [70] Hiller K H 1964 Strength reduction and length changes in porous glass caused by water vapor adsorption *J. Appl. Phys.* **35** 1622–8
- [71] Mason G 1982 The effect of pore space connectivity on the hysteresis of capillary condensation in adsorption-desorption isotherms *J. Coll. Interface Sci.* **88** 36–46